

Fragment-Based Design of a Potent MAT2a Inhibitor and *in Vivo* Evaluation in an MTAP Null Xenograft Model

Claudia De Fusco,\* Marianne Schimpl,\* Ulf Börjesson, Tony Cheung, Iain Collie, Laura Evans, Priyanka Narasimhan, Christopher Stubbs, Mercedes Vazquez-Chantada, David J. Wagner, Michael Grondine, Matthew G. Sanders, Sharon Tentarelli, Elizabeth Underwood, Argyrides Argyrou, James M. Smith, James T. Lynch, Elisabetta Chiarparin, Graeme Robb, Sharan K. Bagal, and James S. Scott

Cite This: <https://doi.org/10.1021/acs.jmedchem.1c00067>

Read Online

ACCESS |



Metrics &amp; More

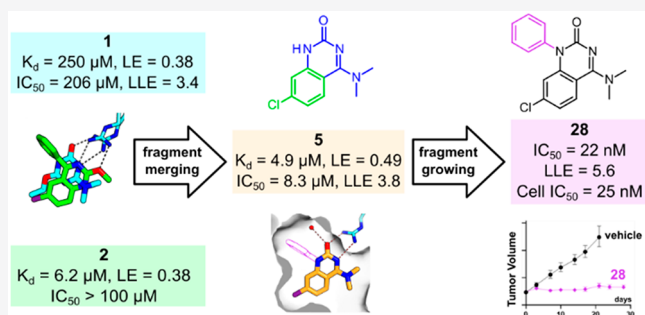


Article Recommendations



Supporting Information

**ABSTRACT:** MAT2a is a methionine adenosyltransferase that synthesizes the essential metabolite S-adenosylmethionine (SAM) from methionine and ATP. Tumors bearing the co-deletion of p16 and MTAP genes have been shown to be sensitive to MAT2a inhibition, making it an attractive target for treatment of MTAP-deleted cancers. A fragment-based lead generation campaign identified weak but efficient hits binding in a known allosteric site. By use of structure-guided design and systematic SAR exploration, the hits were elaborated through a merging and growing strategy into an arylquinazolinone series of potent MAT2a inhibitors. The selected *in vivo* tool compound **28** reduced SAM-dependent methylation events in cells and inhibited proliferation of MTAP-null cells *in vitro*. *In vivo* studies showed that **28** was able to induce antitumor response in an MTAP knockout HCT116



to induce antitumor response in an MTAP knockout HCT116

## INTRODUCTION

The methionine adenosyltransferases MAT1a and MAT2a synthesize the key cofactor S-adenosylmethionine (SAM) from methionine and ATP and play an important role in cellular growth and survival.<sup>1</sup> In adults, MAT1a is primarily expressed in the liver and plays an important role in metabolizing the bulk of dietary methionine. In contrast, MAT2a is mainly expressed in extrahepatic tissues and its expression in the liver is primarily limited to cases of cellular dedifferentiation, such as in fetal liver, or upon liver injury or hepatocellular carcinoma (HCC).<sup>2</sup> A link between MAT2a and other cancers was demonstrated when a shRNA screen in 390 cancer cell lines identified MAT2a knockdown, along with knockdown of PRMT5 and PRMT5 cofactors, as synthetic lethal in MTAP-deficient cancer cells.<sup>3,4</sup> Marjon and colleagues demonstrated *in vivo* that an inducible knockdown of MAT2a reduced tumor growth in an MTAP null MCF7 tumor model.<sup>5</sup>

The MTAP gene is colocalized on chromosome 9p21 with the p16 gene (MTS1/CDK4I/CDKN2A), and homozygous co-deletion of MTAP and p16 genes occurs in 80–90% of tumors with p16 deletion.<sup>6</sup> p16/CDKN2 deletion is among the most frequent cancer-driving mutations, but targeting a loss of function mutant is not trivial due to the lack of a

target protein. The co-deletion of MTAP gene and resulting sensitization to MAT2a inhibition represent a tremendous opportunity to circumvent this issue and provide an option for therapeutic intervention. MTAP-deficient cancer cells are unable to metabolize methylthioadenosine (MTA) as part of the methionine salvage pathway<sup>7</sup> and thereby accumulate intracellular MTA, a potent and selective inhibitor of the methyl transferase PRMT5.<sup>4</sup> This inhibition renders these cancer cells vulnerable to further PRMT5 inhibition either directly or indirectly through inhibition of the upstream metabolic enzyme MAT2a.

Few MAT2a inhibitors were known until very recently. Methionine analogues have been reported as inhibitors of SAM synthesis,<sup>8,9</sup> but being amino acid mimetics and having low potency have limited their applicability. The first drug-like MAT2a inhibitor described in the literature was PF-9366 (Figure 1C).<sup>10</sup> Its binding mode was characterized by X-ray

Received: January 14, 2021

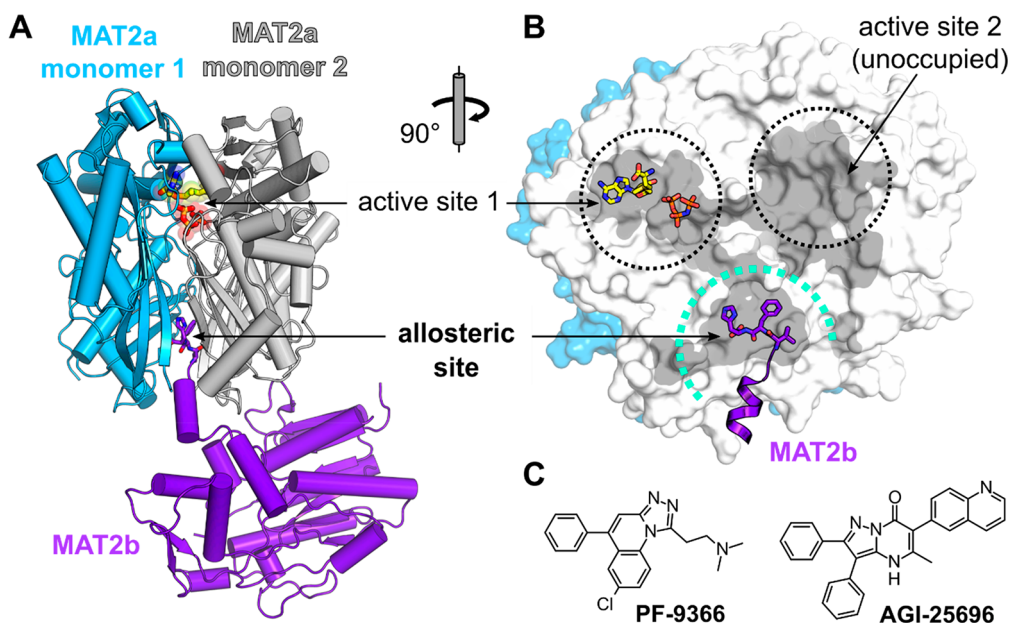


**Figure 1.** MAT2a is a functional homodimer with two catalytic sites and a site of allosteric regulation located at the dimer interface. (A) The two MAT2a monomers are depicted as cartoon in blue and gray. At the interface, the reaction products *S*-adenosylmethionine (*SAM*) and ( $\beta$ - $\gamma$ -imido)triphosphate are captured in one of the two active sites (sticks with yellow carbons). Binding of the carboxy-terminal peptide of MAT2b (purple cartoon) to the dimer interface leads to allosteric regulation of *SAM* biosynthesis (PDB code 4ndn, chains A, B, E). (B) Surface view of MAT2a. Gray shading depicts cavities at the dimer interface, and the largest of these harbor the active and allosteric sites. (C) Recently reported allosteric inhibitors of MAT2a.

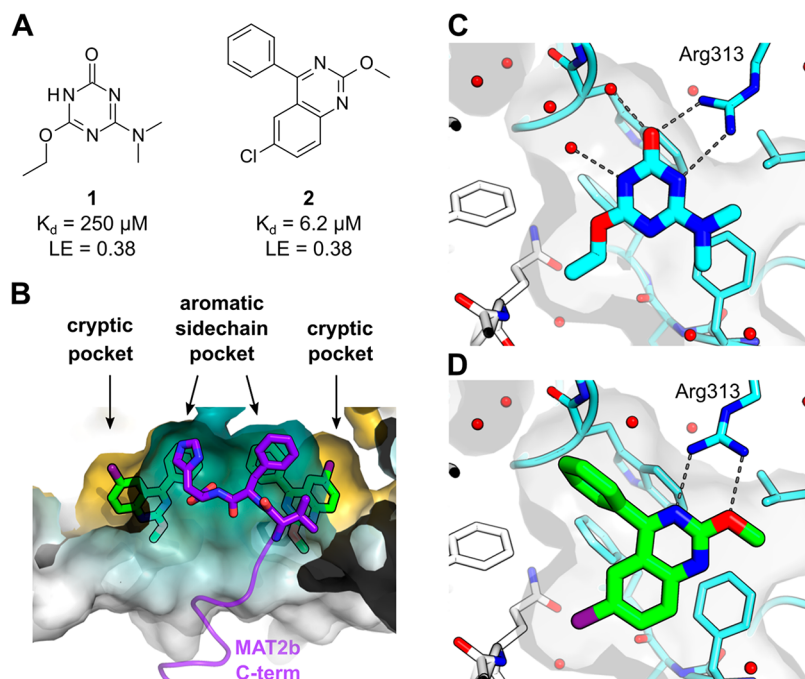


**Figure 2.** Fragment binding induces changes in the allosteric site. (A) Fragment hits 1 and 2 and their MAT2a binding affinities as determined by SPR. (B) Crystal structure of 2 (PDB code 7bhs, 1.1 Å) shows two molecules of the ligand (green sticks and yellow surface) occupying the symmetric site at the dimer interface. Overlay of the MAT2b-bound state (purple sticks and turquoise surface) illustrates the cryptic pocket accessed by small-molecule ligands. (C, D) Close-up view of the binding site and interactions formed by triazinone hit 1 (cyan, PDB code 7bhr, 1.1 Å) and quinazoline hit 2 (green, PDB code 7bhs, 1.1 Å) with Arg313.

crystallography, which revealed that PF-9366 acted as an allosteric inhibitor binding at the interface of two MAT2a subunits, at a site of regulatory control otherwise occupied by the regulatory subunit MAT2b (Figure 1).<sup>11</sup> The authors showed target engagement for PF-9366 and that the

compound was able to modulate *SAM* synthesis in cancer cells with an  $IC_{50}$  of 1.2  $\mu\text{M}$ . However, this did not translate to inhibition of cell proliferation. The upregulation of MAT2a gene expression as a feedback mechanism to MAT2a inhibition was suggested to be the cause of lack of translation.

However, given the weak cell potency of PF-9366, the question remained if a more potent compound would be able to overcome the effect of the feedback loop and MAT2a upregulation. In 2017 Agios disclosed their *in vivo* tool AGI-25696 (Figure 1C) and its related chemical series in a number of patents,<sup>12–14</sup> and in the following year, the first clinical trial with a MAT2a inhibitor, AG-270, was opened, enrolling patients with advanced solid tumors or lymphomas with homozygous MTAP deletion.

This paper describes a fragment-based approach to discovering new MAT2a inhibitors. Several marketed drugs and a growing number of clinical candidates have been generated by fragment-based drug discovery, which is based on the identification of small but efficient hits through highly sensitive and robust biophysical methods.<sup>15,16</sup> One of the underlying principles is the efficient sampling of chemical space by screening molecules with restricted molecular weight. Consequently, the most productive ligand–protein interactions and binders with high ligand efficiency can be identified.<sup>17</sup> With high quality binders in hand and relying heavily on structure-based design, it is possible via strategies of fragment merging or linking to combine desirable features and to generate more complex and higher affinity compounds. Hits can also be expanded by adding atoms or functional groups to target new interactions and/or fill available subpockets (growing).<sup>18</sup> Evolution of the hits through merging, linking, and growing strategies can effectively provide advanced leads while closely controlling the physicochemical properties.

A biophysical fragment screen against MAT2a identified two highly efficient hits binding in the allosteric site. These fragments were merged to generate a new core characterized by higher ligand efficiency and able to inhibit the catalytic activity of MAT2a. A growing strategy was then adopted, resulting in compound 28, which is a potent and orally bioavailable compound that was used to investigate the effect of MAT2a inhibition *in vivo*.

## RESULTS AND DISCUSSION

**Fragment Screening and Hits.** The hit finding strategy comprised three parallel screening approaches: high throughput thermal shift/differential scanning fluorimetry assay of the AstraZeneca fragment library, surface plasmon resonance (SPR) of a high solubility subset of the library, and a cocktail-based crystallographic screen of a different subset. Each of these methods yielded a number of hits that were validated in the screening cascade (data not shown). The most potent and efficient hits originated from the SPR screen and were triazinone 1 and quinazoline 2 with respective affinities of 250  $\mu\text{M}$  and 6.2  $\mu\text{M}$  in SPR and high ligand efficiency (LE) of 0.38 for both. Given the low  $\log D_{7.4}$  (0.23) of compound 1, its lipophilic ligand efficiency (LLE) was a promising 3.4, and overall 1 was deemed a good starting point for a hit-to-lead campaign (Figure 2A). Quinazoline 2 was a highly lipophilic compound, with a  $\log D_{7.4}$  of 4.1 and a LLE of 1.1. Crystal structures were obtained of MAT2a in complex with the fragment hits, showing that they bound in the same site as the regulatory subunit MAT2b. This site has two identical halves, being located at the dimer interface and on the rotational 2-fold axis of cyclic C2 symmetry (Figures 1 and S1). While MAT2b binds once per dimer in a 1:2 molar ratio, small-molecule ligands bound with 1:1 stoichiometry, each ligand

occupying one-half of the binding site (Figure 2B). Ligand binding caused the side chain of Phe333 to rotate by 180°, reshaping the site from a short and wide pocket to a long and narrow cleft. In its new orientation, Phe333 partially occluded solvent access (Figure S1). Moreover, the position vacated by this side chain formed a cryptic pocket occupied by the ethoxy group of 1 and the chlorine of 2 (Figure 2B–D).

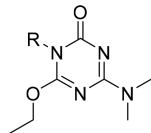
Both fragments formed a bidentate interaction with Arg313 (Figure 2C,D), which assumed slightly different conformations in the two crystal structures. The smaller compound, 1, protruded into the cryptic pocket with its ethoxy substituent, while the dimethylamine pointed toward solvent. There was an additional contact to a water molecule in the subsite that harbors a His or Phe side chain in the MAT2b complex with the dimeric MAT2a (“aromatic side chain pocket”, Figure 2B). Compound 2 displaced this water and occupied the subsite with a phenyl moiety while positioning a chlorine in the cryptic pocket. Given that this site ordinarily harbors a phenylalanine side chain, it offers predominantly lipophilic contacts.

It was important to determine whether binding of compounds at the allosteric site translated to inhibition of enzyme activity. The hits were, therefore, further characterized in an enzymatic functional assay; the assay followed the formation of free phosphate (Experimental Section), which is a product of the ATP dependent MAT2a-catalyzed reaction converting methionine to SAM (eq S1).

Despite its small size and modest affinity, 1 showed inhibition with an  $\text{IC}_{50}$  of 206  $\mu\text{M}$ , which correlated well with its binding affinity, while 2 was surprisingly inactive in this assay.

**Initial SAR and Fragment Merging.** Initial exploration of triazinone 1 showed a very tight SAR, with close analogues having no affinity for MAT2a. Key compounds are summarized in Table 1. Methylation of the triazinone NH

Table 1. Initial SAR Exploration around Hit 1



compd	R	$\log D_{7.4}$ <sup>a</sup>	$K_d$ ( $\mu\text{M}$ ) <sup>b</sup>	LE <sup>c</sup>	$\text{IC}_{50}$ ( $\mu\text{M}$ ) <sup>b</sup>	LLE <sup>d</sup>
1	H	0.23	250	0.38	206	3.4
3	Me	0.66	>200		>1000	
4	Ph	1.1	40	0.32	307	2.4

<sup>a</sup> $\log D_{7.4}$  determined by shake flask method. <sup>b</sup>All  $K_d$  and  $\text{IC}_{50}$  data are the mean values of at least  $n \geq 3$  independent measurements. Each has a SD  $\pm 0.3$  log units unless otherwise noted. See Supporting Information for details. <sup>c</sup>Ligand efficiency (LE) =  $1.4 \cdot \text{p}K_d / (\text{heavy atom count})$ . <sup>d</sup>Lipophilic ligand efficiency (LLE) =  $\text{pIC}_{50} - \log D_{7.4}$ .

in 3 led to loss of binding, likely due to the perturbation of the water network and the inefficient filling of the aromatic side chain pocket. Conversely, a much bigger phenyl substituent in compound 4 was tolerated and led to a ~6-fold increase in binding affinity ( $K_d = 40 \mu\text{M}$  vs 250  $\mu\text{M}$  of the initial hit), but unexpectedly, this did not translate into an increase in functional activity.

Following these initial findings, a different core was proposed based on the overlay of the two fragment hits 1 and 2 (Figure 3). This new core, 2-quinazolinone 5, not only

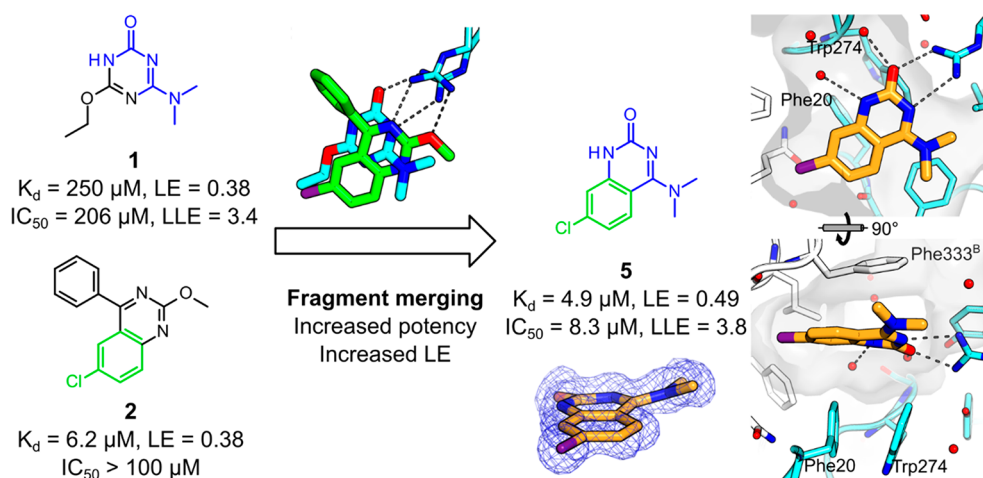


**Figure 3.** Merging strategy from hits 1 and 2 to quinazolinone 5. Binding mode confirmed by crystallography (PDB code 7bht, 1.1 Å) shows that key interactions are maintained, notably the bidentate hydrogen bonding to Arg313 and hydrophobic stacking with Phe333. Compound 5 is visibly nonplanar as seen in the electron density (blue mesh shows  $2F_o - F_c$  map contoured at  $1\sigma$ ); see also Figure S3.

maintained the binding affinity of the most potent of the two hits but also had a much better ligand efficiency due to its small size (LE = 0.49 vs 0.38 of each of the two hits). Moreover, 5 had a significant improvement in inhibitory potency of 8.3  $\mu\text{M}$  and given its  $\log D_{7.4}$  of 1.3 had a promising LLE of 3.8. The quinazolinone was found to bind as expected, maintaining the bidentate interaction of 1 with Arg313 and occupying more fully the lipophilic cryptic pocket where the ethoxy substituent of 1 was located. The Phe333 side chain displaced from this site participated in a hydrophobic stacking interaction with the ligand, concomitantly shielding the compound from solvent. The ligand participated in two additional  $\pi$ -stacking interactions with the side chains of Phe20 and Trp274. The crystal structure also clearly showed a distinct divergence from planarity in this compound, with the dimethylamine group on the one hand, and the carbonyl O atom on the other, being on opposite sides of the extended plane of the phenyl ring (Figure 3). This substituent effect on aromatic ring conformation appeared to originate from steric interaction between the aromatic CH in position 5 and the alkylamine substituent in position 4.

The binding site of 5 was analyzed computationally by characterizing putative water sites using the software WaterMap<sup>19,20</sup> (Figure S2). Three water sites, corresponding to the crystallographic waters seen near N1, were determined computationally to have excess free energies  $\Delta G$  significantly greater than 0 compared to bulk water (i.e., “unstable”). The water site nearest N1, at about 3.4 Å distance, had the greatest calculated excess free energy ( $\Delta G = +6.8$  kcal/mol) and was potentially displaceable by substitution off the N1 position.

**SAR Understanding of the Quinazolinone Core and Fragment Growing.** With this new core in hand, the first step was to understand the key pharmacophoric elements. The chlorine and the dimethylamine substituents were both found to be essential for activity, with compounds 6 and 7 being inactive (Table 2). Methylamine 8 lost activity ( $\text{IC}_{50} = 55$   $\mu\text{M}$ ), and primary amine 9 was completely inactive. Acetylating the amine (compound 10) was not tolerated. The O-linked compounds (11 and 12) and the phenyl analogue 13 were also inactive. This could be due to a combination of

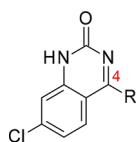
**Table 2.** Key SAR around the Quinazolinone Core and Alternative 4-Substituents<sup>a</sup>

compd	R	$\log D_{7.4}$	$\text{IC}_{50}$ ( $\mu\text{M}$ )	LLE
5	N(Me) <sub>2</sub>	1.3	8.3	3.8
6		0.4	>100	
7	H	1.7	>100	
8	NHMe	1.6	55	2.7
9	NH <sub>2</sub>	1.2	>100	
10	NHAc	1.3	>100	
11	OMe	2.0	>100	
12	OPh	2.7	>100	
13	Ph	2.4	>100	

<sup>a</sup>Legend as in Table 1.

reasons, ranging from disrupting the water network around the Arg313, steric clashes, and/or the inability of the compounds to adopt a nonplanar conformation similar to that of compound 5 (Figure 3).

Further investigation focused on exploring the tertiary amine SAR, and the results are summarized in Table 3. Compound 14 bearing a methylethylamine substituent showed an improvement in both potency and LLE compared to 5 ( $\text{IC}_{50} = 0.74$   $\mu\text{M}$ , LLE = 4.4 vs  $\text{IC}_{50} = 8.3$   $\mu\text{M}$ , LLE = 3.8). In an attempt to make an interaction with Glu342, a base was appended to the ethyl substituent (15), but this change abolished all activity. An N-linked phenyl substituent was not tolerated (16), while N-benzyl 17 had some residual activity but was ~10-fold weaker than the starting point and with a much lower LLE. An ethyl linker to the Ph resulted in a complete loss of potency (18). Cyclic amines were then investigated, and while the azetidine 19 was inactive, the larger pyrrolidine substituent in 20 had a similar activity to 5. A contributing factor to this piece of SAR may be the peculiar substituent effect on the conformation of the quinazolinone ring system. Quantum-mechanical calculations

Table 3. Fragment Growth from the Tertiary Amine in Position 4<sup>a</sup>

compd	R	log $D_{7.4}$	IC <sub>50</sub> ( $\mu$ M)	LLE
5		1.3	8.3	3.8
14		1.8	0.74	4.4
15		-0.50	>100	-
16		2.8	>100	-
17		2.9	81	1.1
18		3.1	>100	-
19		1.8	>100	-
20		1.8	5.0	3.5
21		2.4	75	1.7
22		0.11	52	4.2
23		0.97	>100	-
24		2.9	>100	-

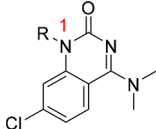
<sup>a</sup>Legend as Table 1.

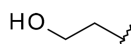
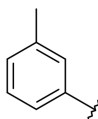
suggested that the active compounds **5** and **20** had energy minima that involve a clear divergence from planarity of the quinazolinone ring system and substituents being partially out-of-plane (as observed by X-ray for **5** bound to MAT2a and described above; Figure 3), while the inactive **19** had an essentially flat predicted minimum-energy conformation with

coplanar substituents (Figure S3). The observed out-of-plane conformations of **5** and **20** may therefore contribute favorably to their binding to MAT2a. Despite comparable activity to compound **5**, pyrrolidine **20** had a higher log  $D_{7.4}$  and a slightly lower LLE of 3.5. Both increasing the size of the ring to six atoms (**21**) or substitution of the 5-membered ring (**22**, **23**, and **24**) did not improve potency.

Given the encouraging results from expanding triazinone **4** into the aromatic side chain pocket (Table 1), substitution of the endocyclic N became the following area of exploration with data summarized in Table 4.<sup>21</sup> Me-substituted **25** was ~20-fold weaker than the starting point, consistent with the result obtained by methylating the triazinone (**3** vs **1**). As stated before, this was believed to be due to perturbation of the water network and the formation of a high-energy void. In order to compensate for the loss of water-mediated interactions with the pocket, it was envisaged that a hydroxyl group at the right distance would be able to form a hydrogen bond with the backbone carbonyl of Gly273. Gratifyingly, compound **26** was found to be equipotent with **5**, but given its lower log  $D_{7.4}$  its LLE increased to 4.4 compared to 3.8 for **5**, suggesting that the compound was able to efficiently displace the water and form a further productive interaction within the pocket. The crystal structure confirmed this predicted interaction, with the compound adopting two distinct conformations that positioned the hydroxyl within hydrogen bonding distance of Gly273 (Figure 4A). The 'Pr substituent in **27** was also tolerated but did not bring any advantage in terms of potency or efficiency. In the original triazinone core the H to phenyl modification had led to a ~6-fold improvement in affinity but not to an increase in biochemical potency. Conversely, in this elaborated scaffold, the addition of a Ph substituent led to **28** with a biochemical potency of 22 nM and a LLE of 5.6, bringing an almost 400-fold increase in potency compared to the parent **5**. The crystal structure showed the additional ring effectively displacing two water molecules and interacting with Phe333 in a CH- $\pi$  interaction. The greatly enhanced potency and efficiency of **28** can be rationalized in terms of the good complementarity between the ligand and the pocket as well as the low rotational freedom of the ligand in the unbound state. Also, the displacement of two "unstable" water molecules (Figures S2 and 4B) likely contributed to its potency gain. From further analysis of the crystal structure, a small lipophilic pocket was identified and a methyl substituent in the meta position was envisaged to fill it. The resulting compound **29** had a biochemical potency of 16 nM, similar to **28**, but because it was more lipophilic, the LLE was not improved. Given the water network present in the aromatic side chain pocket in the absence of the Ph, it was hypothesized that a nitrogen in the ring could stabilize this network by interacting with one of the waters. 3-Pyridyl **31** was found to be optimal with an IC<sub>50</sub> of 21 nM and an impressive LLE of 6.9. The crystal structure (Figure 4D) showed a perfect overlay with the phenyl analogue **28** and a water-mediated interaction between the pyridine N of the ligand and the protein. The electron-poor nature of the pyridine likely increased the ability of the proton in position 5 to form a weak CH-hydrogen bond with the Gly273 carbonyl group, all contributing to the potency and the efficiency of **31**.

**Activity in Cell and Combination of SAR.** A selection of compounds were profiled in a cellular assay which

Table 4. Growth from Position 1<sup>a</sup>


compd	R	log $D_{7.4}$	IC <sub>50</sub> ( $\mu$ M)	LLE
5		1.3	8.3	3.8
25		1.3	187 <sup>b</sup>	2.4
26		0.76	7.2	4.4
27		1.5	8.9	3.5
28		2.0	0.022	5.6
29		2.4	0.016	5.3
30		0.84	20	3.9
31		0.82	0.021	6.9

<sup>a</sup>Legend as Table 1. <sup>b</sup>Standard deviation is 0.35.

measures symmetric dimethyl arginine (SDMA) levels. Symmetric arginine methylation is a downstream measure of MAT2a activity through PRMT5, which is inhibited by being starved of its substrate SAM. The phenyl quinazolinone **28** showed a potent IC<sub>50</sub> of 25 nM in this assay. Given the promising effect in cells, the following step was to relate MAT2a inhibition to the ability of the compounds to inhibit cellular proliferation. Gratifyingly, compound **28** was able to inhibit proliferation of HCT116 MTAP knockout cells with an IC<sub>50</sub> of 250 nM. Pyridine **31** showed a similar cellular potency and proliferation inhibition for a lower log  $D$ .

A final round of optimization combined the *N*-4-ethyl, identified from compound **14**, with the optimal aryl groups from **28** and **31** generating **32** and **33**, respectively. Both these compounds showed single digit nanomolar potency in cells and proliferation inhibition potencies of 140 nM.

**Pharmacokinetics.** *In vitro* DMPK properties of compounds **28** and **31**—**33** were profiled. These four compounds displayed moderate to high solubility, high permeability, and

low efflux, and they also showed low to moderate human hepatocyte intrinsic clearance (CL<sub>int</sub>) (Table 6) which generally tracked with log  $D$  (Table 5). The compounds were screened for inhibition against a panel of five cytochrome P450 isoforms (CYP1A2, CYP2C9, CYP2C19, CYP2D6, and CYP3A4) in human liver microsomes. Only weak inhibition of CYP1A2 and CYP3A4 was observed for compounds **32** and **33** (Table 6) with all others showing no activity (IC<sub>50</sub> > 30  $\mu$ M). No compound showed activity against the hERG ion channel up to 40  $\mu$ M.

Low to moderate CL<sub>int</sub> values were observed in rat hepatocytes which corresponded to low to moderate *in vivo* rat clearance (noncompartmental) (Table 7). Bioavailability in rat (Table 7) was moderate to high (57–100%) consistent with high absorption expected given the *in vitro* DMPK properties of these compounds. The volume of distribution was generally moderate and consistent with the neutral ion class (0.56–2.1 L/kg). **28** and **31** were selected to be

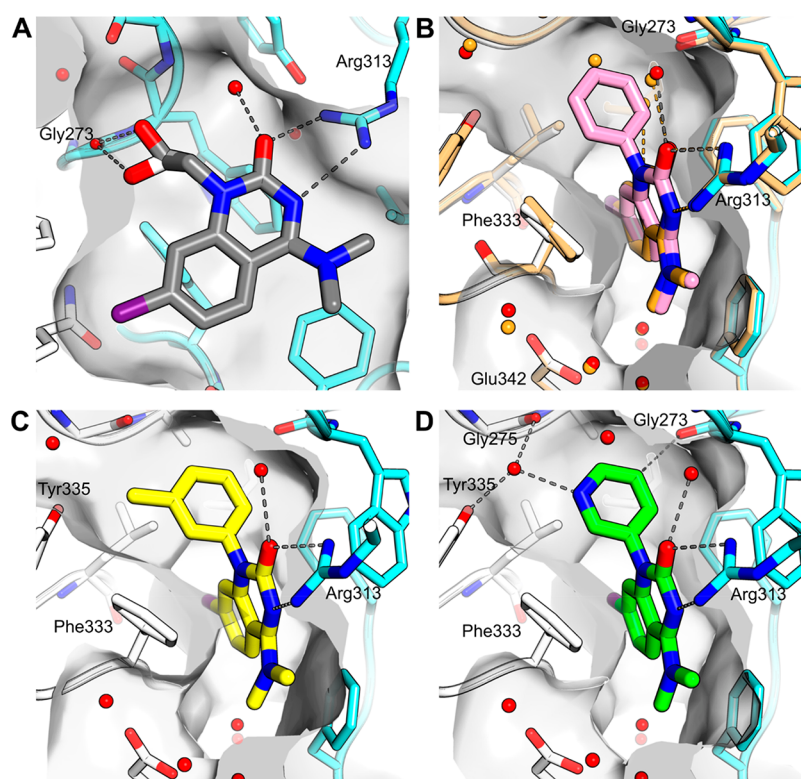
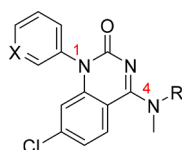


**Figure 4.** Optimization of the substituent occupying the aromatic side chain subsite. (A) The hydroxyethyl substituent in **26** forms a hydrogen bond with the backbone carbonyl of Gly273. Two alternative conformations were observed in the crystal structure, shown as light and dark gray sticks (PDB code 7bhu, 1.2 Å). (B) The phenyl substitution in **28** (pink) brings an almost 400-fold potency boost compared to **5** (orange). The superposition of both crystal structures shows that the phenyl group displaces two water molecules. The side chain of Phe333 undergoes a slight rotation, maximizing a CH- $\pi$  interaction (PDB code 7bhv, 1.2 Å). (C) **29** (yellow, PDB code 7bhw, 1.2 Å) fills a small hydrophobic side pocket with a methyl substituent. (D) **31** (green, PDB code 7bhx, 1.1 Å) features a pyridine to capture a water interaction. A weak CH-hydrogen bond to Gly273 is indicated by gray dashes.

**Table 5. Combination of Substituents in Positions 1 and 4<sup>a</sup>**



compd	R	X	log $D_{7.4}$	IC <sub>50</sub> ( $\mu$ M)	LLE	cell IC <sub>50</sub> ( $\mu$ M)	prolif IC <sub>50</sub> ( $\mu$ M)
28	Me	C	2.0	0.022	5.6	0.025	0.25
31	Me	N	0.82	0.021	6.9	0.017	0.33
32	Et	C	2.5	0.013	5.4	0.0063	0.14
33	Et	N	1.2	0.018	6.5	0.0052	0.14 <sup>b</sup>

<sup>a</sup>Legend as Table 1. <sup>b</sup>Average of two repeats.

evaluated in mouse pharmacokinetic studies to understand suitability for pharmacodynamic studies.

Unfortunately, *in vitro* mouse metabolism was much higher than rat or human for these compounds, which correlated with much higher mouse *in vivo* clearance when compared with rat (Table 7). Due to the higher mouse clearance, both subcutaneous (sc) dosing and oral (po) dosing of **28** and **31** were evaluated at high doses to enable *in vivo* efficacy studies (Figure 5). The lower solubility of **28** relative to **31** (103 vs >1000  $\mu$ M) allowed for a suspension SC formulation (0.5% w/v hydroxypropylmethylcellulose/0.1% w/v Tween 80) which displayed dissolution rate limited kinetics that

prolonged plasma half-life and lowered  $C_{max}$ . Conversely, **31** displayed rapid absorption from both sc and po administration displaying similar profiles due to higher solubility as solution formulations (Figure 5). Due to the favorable PK profile of sc dosing **28**, this compound and formulation were progressed to target engagement and efficacy studies. 50 mg/kg sc dosing of **28** was utilized in target engagement and efficacy studies after observing similar exposure and prolonged half-life at both 50 mg/kg and 100 mg/kg sc after repeat dosing (Figure S4).

**In Vivo Target Engagement and Efficacy.** *In vivo* profiling of **28** was carried out through an efficacy study in an HCT116 MTAP knockout xenograft tumor model. 50 mg/kg of **28** was administered once daily sc to female Ncr nude mice and resulted in an average reduction of tumor SAM concentration by 74% compared to vehicle control (0.5% w/v HPMC/0.1% w/v Tween 80) (Figure 6A). Consequently, a significant antitumor response was observed leading to tumor stasis (Figure 6B, left). However, while compound **28** was tolerated over the course of the 28 day treatment, mice did exhibit a maximum body weight loss of 8% (Figure 6B, right).

**Synthesis of Selected Compounds.** Quinazolinone **5** was prepared by  $S_NAr$  reaction on 2,4,7-trichloroquinazoline **5a** with dimethylamine, followed by hydrolysis with acetic acid (Scheme 1).

Quinazolinones **28** and **31–33** were synthesized as shown in Scheme 2. Commercial 4-chloro-2-fluorobenzamide was

Table 6. *In Vitro* Human DMPK Properties

compd	human hep CL <sub>int</sub> ( $\mu\text{L}/\text{min}$ )/ $10^6$ cells <sup>a</sup>	human % free <sup>b</sup>	Caco2 P <sub>app</sub> /ER <sup>c</sup>	solubility $\mu\text{M}$ <sup>d</sup>	IC <sub>50</sub> ( $\mu\text{M}$ )		
					CYP3A4 <sup>e</sup>	CYP1A2 <sup>e</sup>	hERG <sup>f</sup>
28	11	13	29/0.97	103	>30	>30	>40
31	<1	64	64/1.6	>1000	>30	>30	>40
32	18	8.1	73/0.86	220	>30	18	>40
33	3.4	35	44/2.2	930	24	>30	>40

<sup>a</sup>Rate of metabolism ( $(\mu\text{L}/\text{min})/10^6$  cells) determined from DMSO stock solution in isolated hepatocytes diluted to  $10^6$  cells/mL. <sup>b</sup>Determined from DMSO stock solution by equilibrium dialysis in 10% human plasma supplied by BioreclamationIVT. <sup>c</sup>Compounds were incubated at  $10 \mu\text{M}$  in cultured Caco2 cells. Intrinsic permeability was measured in units of  $\times 10^{-6}$  cm/s in the apical direction in the presence of transport inhibitors quinidine ( $50 \mu\text{M}$ ), sulfasalazine ( $20 \mu\text{M}$ ), and benzbromarone ( $30 \mu\text{M}$ ) with an apical/basolateral pH of 6.5:7.4, respectively. Efflux ratio is reported as the ratio of basolateral (B to A) to apical (A to B) transport in the absence of any inhibitors and an apical/basolateral pH of 7.4:7.4. <sup>d</sup>Solubility of compounds in aqueous phosphate buffer at pH 7.4 after 24 h at  $25^\circ\text{C}$  from DMSO stock solution. <sup>e</sup>Inhibition of cytochrome P450 enzymes IC<sub>50</sub>. <sup>f</sup>Inhibition of the hERG tail current was measured using a plate-based planar patch clamp system (Syncropatch).

Table 7. *In Vitro* and *in Vivo* Rodent DMPK Properties<sup>a</sup>

compd	species	CL <sub>int</sub> ( $(\mu\text{L}/\text{min})/10^6$ cells)	% free	Cl ( $(\text{mL}/\text{min})/\text{kg}$ )	V <sub>ss</sub> (L/kg)	T <sub>1/2</sub> (h)	F (%)
28	rat	4.6	10	16	0.85	1.2	100
31	rat	1.3	45	19	2.1	3.6	100
32	rat	13	3.7	12	0.43	1.1	100
33	rat	3.9	20	6.6	0.56	3.4	57
28	mouse	67	13	109	1.0	0.25	25
31	mouse	14	56	62	2.2	3.7	79

<sup>a</sup>Compound was dosed in rat intravenously at 0.5 and orally at 1 mg/kg. The formulation was 5% DMSO/95% hydroxylpropyl  $\beta$ -cyclodextrin (30% w/v) at a volume of 1 mL/kg and 4 mL/kg, iv and po, respectively.

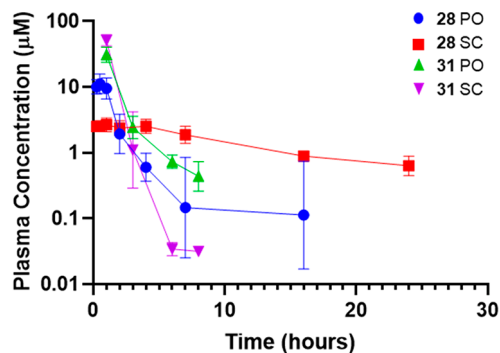
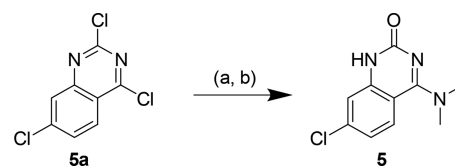


Figure 5. Mouse plasma concentrations of 28 po (blue circle), 28 sc (red square), 31 po (green triangle), and 31 sc (purple triangle) at 100 mg/kg.

treated with oxalyl chloride to form the isocyanate *in situ*. The reaction was then cooled to room temperature and the corresponding aniline added to form acyl ureas 34a and 34b.

Scheme 1. Synthesis of 5<sup>a</sup>

<sup>a</sup>Reagents and conditions: (a) dimethylamine, THF, rt, 2 h; (b) acetic acid,  $100^\circ\text{C}$ , 12 h, 29% over two steps.

Intermediate 34 was carried through to the next step, together with an oxalamide byproduct impurity (approximately 20–25%) identified after purification. A KHMDS-mediated cyclization of 34 was used to generate the quinazolinone ring (intermediates 35a and 35b). PyBOP coupling with the corresponding amine completed the synthesis of the desired compounds 28, 31, 32, and 33 in respectable yields (50–92%).

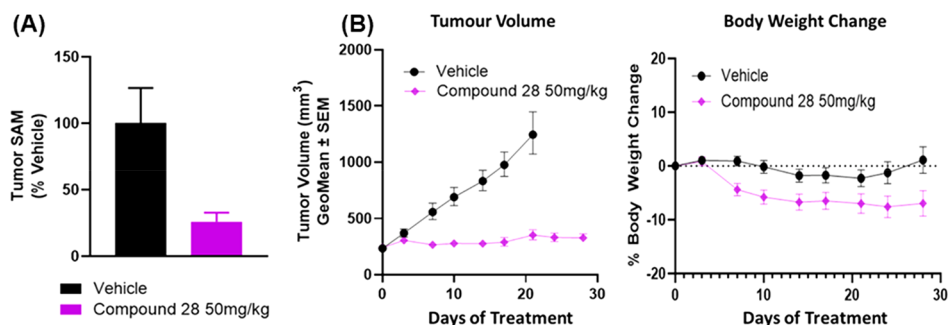
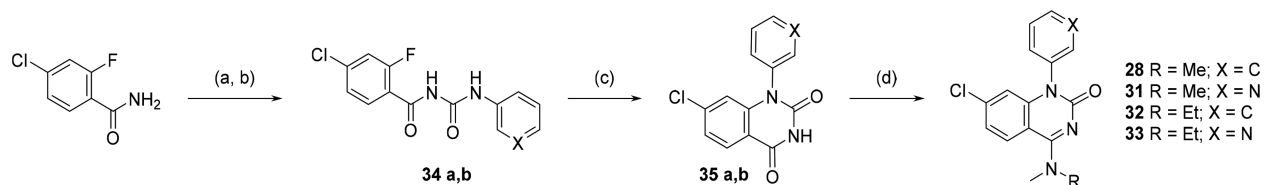


Figure 6. Subcutaneous dosing of 28 at 50 mg/kg QD: (A) reduction in tumor SAM; (B) antitumor response (left) and body weight change (right).

Scheme 2. Synthesis of 28, 31, 32, and 33<sup>a</sup>

<sup>a</sup>Reagents and conditions: (a) oxalyl chloride, DCE, 80 °C, 30 min; (b) aniline, rt, 1 h, 62–75% over two steps; (c) KHMDS, THF, –78 °C, 1 h, then rt, 3.5 h, 67–80%; (d) PyBOP, DBU, amine, MeCN, rt, 2.5 h, 50–92%.

## CONCLUSIONS

A series of MAT2a inhibitors was developed originating from weak fragment hits through a structure-based merging strategy. This led to quinazolinone **5** which was a low molecular weight, potent, and efficient compound and formed the basis for further optimization. By use of structure-based design, fragment growing led to compounds with over 1000-fold improvement in potency over the original fragment hits together with excellent physicochemical properties. Arylquinazolinones **28** and **31–33** showed inhibition of PRMT5-mediated symmetric dimethylation of arginine (SDMA) and antiproliferative activity in MTAP null cells. Compound **28** was identified as a promising *in vivo* tool that exhibited reduction in tumor SAM levels and antitumor response in an MTAP knockout HCT116 xenograft model.

## EXPERIMENTAL SECTION

Unless otherwise stated, commercially available reagents were used as supplied. Preparative reverse phase HPLC was performed on an Agilent 1290 Infinity II Preparative system equipped with a SQ MS detector (multimode ESI/APCI source), with a Waters CSH C18 OBD column (5 μm silica, 30 mm diameter, 100 mm length, flow rate of 50 mL/min) using decreasingly polar mixtures of water (containing 0.1–0.3% aqueous ammonium) or water (containing 0.1% formic acid) and acetonitrile as eluents. Preparative SFC purification was performed on either a Sepiatec P100 SFC system or Waters Prep 100 SFC system equipped with QDa MS detector, using the chromatographic conditions as detailed in corresponding experimental data. Proton magnetic resonance spectra were determined using a Bruker Avance 500 (500 MHz) and Bruker Avance 400 (400 MHz) instruments and were determined in CDCl<sub>3</sub>, DMSO-*d*<sub>6</sub>, or MeOH-*d*<sub>4</sub>. Measurements were taken at ambient temperature unless otherwise specified. The following abbreviations have been used: s, singlet; d, doublet; t, triplet; q, quartet; m, multiplet; dd, doublet of doublets; ddd, doublet of doublets of doublets; dt, doublet of triplets; tt, triplet of triplets; bs, broad signal. End products were also characterized by mass spectrometry following liquid chromatography (LCMS or UPLC). Reverse-phase C18 silica was used with a flow rate of 1 mL/min, and detection was by electrospray mass spectrometry and by UV absorbance recording a wavelength range of 220–320 nm. Analytical UPLC was performed on CSH C18 reverse-phase silica, using a Waters Acquity UPLC CSH C18 column with dimensions 2.1 mm × 50 mm and particle size 1.7 μm. Gradient analysis was employed using decreasingly polar mixtures as eluent, for example, decreasingly polar mixtures of water (containing 0.1% formic acid or 0.1% ammonia) as solvent A and acetonitrile as solvent B. A typical 2 min analytical UPLC method would employ a solvent gradient over 1.3 min, at approximately 1 mL/min, from a 97:3 mixture of solvents A and B respectively to a 3:97 mixture of solvents A and B. The reported molecular ion corresponds to the [M + H]<sup>+</sup> unless otherwise specified. For molecules with multiple isotopic patterns (Br, Cl, etc.) the reported value is the one obtained for the lowest isotope mass unless otherwise specified. Purities were assessed using

LCMS by UV absorbance and <sup>1</sup>H NMR and are ≥95% for screening compounds.

**4-Chloro-2-fluoro-N-(phenylcarbonyl)benzamide (34a).** To a stirred suspension of 4-chloro-2-fluorobenzamide (10.0 g, 57.6 mmol) in DCE (200 mL) at rt was added oxalyl dichloride (5.36 mL, 63.4 mmol). The resultant suspension was heated to 80 °C for 30 min. The reaction mixture was allowed to cool to rt, and aniline (10.5 mL, 115 mmol) was added to the reaction mixture (on addition a suspension formed). The resultant reaction mixture was stirred at rt for 1 h. The reaction mixture was cooled using an ice bath and was then quenched by carefully pouring into a saturated aqueous solution NaHCO<sub>3</sub> (1 L). This was stirred for approximately 10 min. The precipitate was collected by filtration, washed with water (1 L), and dried under vacuum to afford 4-chloro-2-fluoro-N-(phenylcarbonyl)benzamide **34a** (75% pure; 16.8 g, 99%) as a white solid. <sup>1</sup>H NMR (400 MHz, DMSO): 7.12 (tt, *J* = 7.8, 1.1 Hz, 1H), 7.31–7.4 (m, 2H), 7.41–7.48 (m, 1H), 7.52–7.6 (m, 2H), 7.63 (dd, *J* = 10.3, 1.9 Hz, 1H), 7.68–7.77 (m, 1H), 10.37 (s, 1H), 11.06 (s, 1H). *m/z*: ES+ [M + H]<sup>+</sup> 293.

**7-Chloro-1-phenylquinazolin-2,4(1H,3H)-dione (35a).** To a stirred white suspension of 4-chloro-2-fluoro-N-(phenylcarbonyl)benzamide **34a** (75% pure; 16.8 g, 43.0 mmol) in anhydrous THF (100 mL) under a nitrogen atmosphere at –78 °C was added KHMDS (126 mL, 1 M in THF solution, 126 mmol) dropwise. On addition, the reaction mixture turned an orange color. The reaction mixture was stirred at –78 °C for 1 h and then warmed to rt for 3.5 h. The reaction mixture was slowly quenched with saturated aqueous NH<sub>4</sub>Cl solution. A precipitate was formed to give a thick suspension, which was filtered and washed with water to afford the crude product. The crude product was stirred in approximately 200 mL of water for 30 min. The white suspension was filtered, washing the solids with water, dried under vacuum at 50 °C to afford 7-chloro-1-phenylquinazolin-2,4(1H,3H)-dione **35a** (85% pure; 14.7 g, 80%) as a white solid. <sup>1</sup>H NMR (400 MHz, DMSO): 6.32 (d, *J* = 1.8 Hz, 1H), 7.31 (dd, *J* = 8.4, 1.9 Hz, 1H), 7.42–7.5 (m, 2H), 7.53–7.68 (m, 3H), 8.01–8.08 (m, 1H), 11.79 (s, 1H). *m/z*: ES– [M – H]<sup>–</sup> 271.

**7-Chloro-4-(dimethylamino)-1-phenylquinazolin-2(1H)-one (28).** DBU (11.0 mL, 73.9 mmol) was added dropwise to a stirred suspension of 7-chloro-1-phenylquinazolin-2,4(1H,3H)-dione **35a** (85% pure, 6.77 g, 21.1 mmol), PyBOP (16.5 g, 31.7 mmol), and dimethylamine (26.4 mL, 2 M in THF, 52.8 mmol) in acetonitrile (110 mL) at rt. The resultant suspension was stirred at rt for 2.5 h. Additional PyBOP (4.00 g, 10.6 mmol), dimethylamine (7.0 mL, 2 M in THF, 14 mmol), and DBU (3.0 mL, 20 mmol) were added, and the reaction mixture was left stirring at rt for 30 min. The reaction mixture was concentrated to dryness. The crude mixture was diluted with DCM and washed sequentially with water and saturated brine. The organic layer was dried with a phase separating cartridge, filtered, and concentrated to afford the crude product as a brown oil (approximately 31 g). The crude product was dissolved in acetonitrile (80 mL). A fine white precipitate started to crash out. The suspension was slowly passed through a phase separator cartridge into a stirred flask with water (800 mL). Upon addition a solid precipitated. This was carefully filtered and the solid washed with water. The solid was dried under vacuum at 50 °C to afford the crude product (6.78 g) as a light brown solid. The crude sample

(6.78 g) was dissolved to a concentration of 113 mg/mL in 60 mL of DCM/DMF/DMSO (1:1:1), heated, sonicated, and filtered. The resulting solution was purified by preparative SFC (column, YMC Diol, 30 mm × 250 mm, 5 μm, mobile phase of 15–25% MeOH + 0.1% NH<sub>3</sub>/85–75% scCO<sub>2</sub> over 7 min, 1.5 min flush at 50% MeOH; flow rate of 100 mL/min; BPR, 120 bar; column temperature of 40 °C). Fractions containing the desired product were concentrated to dryness to afford 7-chloro-4-(dimethylamino)-1-phenylquinazolin-2(1H)-one **28** (5.80 g, 92%) as an off white solid. <sup>1</sup>H NMR (400 MHz, DMSO): 3.31 (s, 6H), 6.33 (d, *J* = 2.1 Hz, 1H), 7.19 (dd, *J* = 8.8, 2.1 Hz, 1H), 7.26–7.35 (m, 2H), 7.45–7.56 (m, 1H), 7.60 (ddd, *J* = 7.7, 6.5, 1.3 Hz, 2H), 8.04 (d, *J* = 8.8 Hz, 1H). <sup>13</sup>C NMR (126 MHz, DMSO, 37 °C) δ: 41.3, 108.6, 114.0, 120.3, 128.5, 129.0, 129.4, 129.9, 137.4, 137.6, 146.2, 153.4, 163.5. *m/z*: ES+ [M + H]<sup>+</sup> 300; HRMS (ESI) for C<sub>16</sub>H<sub>14</sub>ClN<sub>3</sub>O (MH<sup>+</sup>) calculated 300.08982; found 300.08911.

**4-Chloro-2-fluoro-*N*-(pyridin-3-ylcarbamoyl)benzamide (34b)**. To a stirred suspension of 4-chloro-2-fluorobenzamide (7.50 g, 43.2 mmol) in DCE (150 mL) at rt was added oxalyl dichloride (4.02 mL, 47.5 mmol). The resultant suspension was heated to 80 °C for 45 min. The reaction mixture was allowed to cool to rt, and pyridin-3-amine (8.13 g, 86.4 mmol) was added. The reaction mixture was then stirred at rt for 4 h. The reaction mixture was cooled using an ice bath, and the resultant suspension was filtered, washing the solids with DCM. The solid was suspended in a mixture of MeOH/DCM (1:1). The suspension was filtered and the solid dried under vacuum to afford 4-chloro-2-fluoro-*N*-(pyridin-3-ylcarbamoyl)benzamide **34b** (85% pure; 9.26 g, 73%) as a white solid. <sup>1</sup>H NMR (400 MHz, DMSO): 7.36–7.5 (m, 2H), 7.64 (dd, *J* = 10.3, 1.9 Hz, 1H), 7.74 (t, *J* = 8.0 Hz, 1H), 8.10 (ddd, *J* = 8.4, 2.6, 1.5 Hz, 1H), 8.35 (dd, *J* = 4.8, 1.4 Hz, 1H), 8.79 (d, *J* = 2.1 Hz, 1H), 10.46 (s, 1H), 11.21 (s, 1H). *m/z*: ES+ [M + H]<sup>+</sup> 294.

**7-Chloro-1-(pyridin-3-yl)quinazoline-2,4(1H,3H)-dione (35b)**. To a stirred solution of 4-chloro-2-fluoro-*N*-(pyridin-3-ylcarbamoyl)benzamide **34b** (85% pure; 9.26 g, 26.8 mmol) in anhydrous THF (80 mL) under a nitrogen atmosphere at –78 °C was added potassium bis(trimethylsilyl)amide (69.4 mL, 1 M in THF, 69.4 mmol) dropwise. On addition the reaction mixture turned a dark brown color. The reaction mixture was stirred at –78 °C for 1 h and then warmed to rt for 18 h. The reaction mixture was slowly quenched with saturated aqueous NH<sub>4</sub>Cl solution during which a solid precipitated to give a thick suspension, which was filtered and washed with acetonitrile to afford the crude product (13.4 g) as an off white solid. The crude product was stirred in water (100 mL) for 30 min. The white suspension was filtered, washing the solids with water and diethyl ether, dried under vacuum at 50 °C to afford 7-chloro-1-(pyridin-3-yl)quinazoline-2,4(1H,3H)-dione **35b** (80% pure; 6.16 g, 84%). <sup>1</sup>H NMR (400 MHz, DMSO): 6.40 (d, *J* = 1.7 Hz, 1H), 7.34 (dd, *J* = 8.4, 1.9 Hz, 1H), 7.68 (ddd, *J* = 8.1, 4.8, 0.8 Hz, 1H), 7.98 (ddd, *J* = 8.1, 2.5, 1.6 Hz, 1H), 8.06 (d, *J* = 8.4 Hz, 1H), 8.68 (dd, *J* = 2.5, 0.7 Hz, 1H), 8.76 (dd, *J* = 4.8, 1.5 Hz, 1H), 11.76 (s, 1H). *m/z*: ES+ [M + H]<sup>+</sup> 274.

**7-Chloro-4-(dimethylamino)-1-(pyridin-3-yl)quinazolin-2(1H)-one (31)**. DBU (1.91 mL, 12.8 mmol) was added dropwise to a stirred suspension of 7-chloro-1-(pyridin-3-yl)quinazoline-2,4(1H,3H)-dione **35b** (80% pure; 1.25 g, 3.65 mmol), PyBOP (2.85 g, 5.48 mmol), and dimethylamine (4.57 mL, 2 M in THF, 9.13 mmol) in acetonitrile (30 mL) at rt. The resulting yellow solution was stirred at rt for 18 h. The reaction mixture was concentrated to dryness. The crude mixture was diluted with DCM and washed sequentially with water and saturated brine. The organic layer was dried with a phase separating cartridge, filtered, and concentrated to dryness to afford the crude product as an orange oil (approximately 4 g). The sample was dissolved in DMSO and purified by preparative SFC (column, YMC Cyano 30 × 250 mm, 5 μm, mobile phase of 10–12% MeOH + 0.1% NH<sub>3</sub>/90–88% scCO<sub>2</sub> over 8 min, 1.5 min flush at 50% MeOH + 0.1% NH<sub>3</sub>; flow rate of 100 mL/min; BPR of 120 bar; column temperature of 40 °C). Fractions containing the desired product were concentrated to

dryness to afford 7-chloro-4-(dimethylamino)-1-(pyridin-3-yl)quinazolin-2(1H)-one **31** (0.945 g, 86%) as a white solid. <sup>1</sup>H NMR (400 MHz, DMSO): 3.32 (s, 6H), 6.38 (d, *J* = 2.1 Hz, 1H), 7.23 (dd, *J* = 8.8, 2.1 Hz, 1H), 7.64 (ddd, *J* = 8.1, 4.8, 0.7 Hz, 1H), 7.84 (ddd, *J* = 8.1, 2.5, 1.6 Hz, 1H), 8.06 (d, *J* = 8.8 Hz, 1H), 8.54 (dd, *J* = 2.5, 0.7 Hz, 1H), 8.71 (dd, *J* = 4.8, 1.5 Hz, 1H). <sup>13</sup>C NMR (126 MHz, DMSO, 37 °C) δ: 41.4, 108.7, 113.9, 120.7, 124.7, 129.6, 134.4, 137.2, 137.7, 146.0, 149.4, 150.0, 153.4, 163.6. *m/z*: ES+ [M + H]<sup>+</sup> 301. HRMS (ESI) for C<sub>15</sub>H<sub>13</sub>ON<sub>4</sub>Cl (MH<sup>+</sup>) calculated 301.08507; found 301.08453.

**7-Chloro-4-(ethyl(methyl)amino)-1-phenylquinazolin-2(1H)-one (32)**. DBU (0.148 mL, 0.99 mmol) was added dropwise to a stirred suspension of 7-chloro-1-phenylquinazoline-2,4(1H,3H)-dione **35a** (85% pure; 95 mg, 0.28 mmol), PyBOP (220 mg, 0.42 mmol), and *N*-methylethanamine (0.061 mL, 0.71 mmol) in acetonitrile (1.0 mL) at rt. The resultant suspension was stirred at rt for 2.5 h. Additional *N*-methylethanamine (0.061 mL, 0.71 mmol), PyBOP (220 mg, 0.42 mmol), and DBU (0.15 mL, 0.99 mmol) were added, and the resultant reaction mixture was stirred at rt for 2 h. The reaction mixture was concentrated to dryness, and the crude residue was diluted with DCM. The organic layer was washed sequentially with water and saturated brine, dried with a phase separating cartridge, filtered, and evaporated to afford the crude product as a brown oil (753 mg). The crude sample (753 mg) was dissolved in DMSO (6 mL) and was purified by preparative HPLC (Waters CSH C18 OBD column, 30 mm × 100 mm id, 5 μm particle size), using decreasingly polar mixtures of water (containing 0.3% NH<sub>3</sub> aq) and MeCN as eluents, followed by a further step using decreasingly polar mixtures of water (containing 0.1% formic acid aq) and MeCN as eluents. Fractions containing the desired product were concentrated to dryness to afford 7-chloro-4-(ethyl(methyl)amino)-1-phenylquinazolin-2(1H)-one **32** (44 mg, 50%) as a white solid. <sup>1</sup>H NMR (500 MHz, DMSO, 37 °C) 1.32 (t, *J* = 7.0 Hz, 3H), 3.30 (s, 3H), 3.71 (q, *J* = 7.0 Hz, 2H), 6.34 (d, *J* = 2.1 Hz, 1H), 7.20 (dd, *J* = 8.8, 2.1 Hz, 1H), 7.27–7.35 (m, 2H), 7.47–7.57 (m, 1H), 7.54–7.65 (m, 2H), 7.97 (d, *J* = 8.8 Hz, 1H). <sup>13</sup>C NMR (126 MHz, DMSO, 37 °C) δ: 12.1, 38.6, 47.0, 108.6, 114.0, 120.4, 128.5, 129.0, 129.1, 129.9, 137.4, 137.6, 146.3, 153.4, 163.0. *m/z*: ES+ [M + H]<sup>+</sup> 314. HRMS (ESI) for C<sub>17</sub>H<sub>16</sub>ON<sub>3</sub>Cl (MH<sup>+</sup>) calculated 314.10547; found 314.10486.

**7-Chloro-4-(ethyl(methyl)amino)-1-(pyridin-3-yl)quinazolin-2(1H)-one (33)**. DBU (0.12 mL, 0.80 mmol) was added dropwise to a stirred suspension of 7-chloro-1-(pyridin-3-yl)quinazoline-2,4(1H,3H)-dione (80% pure; 125 mg, 0.370 mmol), PyBOP (247 mg, 0.480 mmol), and *N*-methylethanamine (0.047 mL, 0.55 mmol) in acetonitrile (3.0 mL) at rt. The resulting yellow solution was stirred at room temperature for 2 h. Additional DBU (0.12 mL, 0.80 mmol) was added, and the reaction mixture was warmed to 50 °C for 10 min. The reaction mixture was concentrated to dryness, and the crude residue was diluted with DCM. The organic was washed sequentially with water and saturated brine, dried with a phase separating cartridge, filtered, and concentrated to dryness to afford the crude product (600 mg). The crude product was dissolved in DMF (2.0 mL) and was purified by preparative HPLC (Waters CSH C18 OBD column, 30 mm × 100 mm id, 5 μm particle size), using decreasingly polar mixtures of water (containing 0.3% NH<sub>3</sub> aq) and MeCN as eluents. Fractions containing the desired compound were concentrated to dryness to afford 7-chloro-4-(ethyl(methyl)amino)-1-(pyridin-3-yl)quinazolin-2(1H)-one **33** (69.0 mg, 60%) as a white solid. <sup>1</sup>H NMR (400 MHz, DMSO): 1.31 (t, *J* = 7.1 Hz, 3H), 3.32 (s, 3H), 3.72 (q, *J* = 7.0 Hz, 2H), 6.38 (d, *J* = 2.1 Hz, 1H), 7.24 (dd, *J* = 8.8, 2.1 Hz, 1H), 7.64 (ddd, *J* = 8.1, 4.8, 0.8 Hz, 1H), 7.85 (ddd, *J* = 8.1, 2.5, 1.6 Hz, 1H), 7.99 (d, *J* = 8.8 Hz, 1H), 8.55 (dd, *J* = 2.5, 0.7 Hz, 1H), 8.71 (dd, *J* = 4.8, 1.5 Hz, 1H). <sup>13</sup>C NMR (126 MHz, DMSO, 37 °C) δ: 12.0, 38.7, 47.0, 108.8, 114.0, 120.8, 124.7, 129.3, 134.4, 137.2, 137.6, 146.0, 149.4, 150.1, 153.4, 163.1. *m/z*: ES+ [M + H]<sup>+</sup> 315. HRMS (ESI) for C<sub>16</sub>H<sub>15</sub>ON<sub>4</sub>Cl (MH<sup>+</sup>) calculated 315.10072; found 315.09995.

**Surface Plasmon Resonance.** SPR experiments were performed using a Biacore 4000, Biacore T200, or Biacore 8K instrument (Cytiva) at 25 °C. A series S sensor chip SA (Cytiva) was docked into the system in 20 mM Bicine-Na, pH 7.5, 100 mM KCl, 5 mM MgCl<sub>2</sub>, 0.1 mM TCEP, 0.05% (w/w) Tween-20, and 2% (v/v) DMSO. The sensor chip surface was conditioned with 3 × 60 s injections of 50 mM NaOH/1 M NaCl at 30 μL/min before capturing biotinylated Avi-MAT2A protein diluted to 100 nM in running buffer on the active flow cells (3000–5000 RU captured). All remaining biotin binding sites were blocked on the active and reference surfaces with a 60 s injection of 100 μM amine-PEG2-biotin (ThermoScientific) in running buffer. Compounds were tested over a suitable dose–response range by either multicycle kinetics or single-cycle kinetics (slowly dissociating compounds).

**Biochemical Assay.** Inhibition of MAT2a activity was determined using BIOMOL GREEN Reagent (Enzo Life Sciences BML-K1102) which measures the free phosphate released during the assay. For protein production, see the [Supporting Information](#). Assays were performed in 384-well plates (Greiner 781101) in 20 μL volume, 1% (v/v) final DMSO concentration and with the following buffer conditions: 50 mM Tris-HCl (pH 7.4), 5 mM MgCl<sub>2</sub>, 100 mM KCl, 1 mM DTT, and 0.01% Brij23. Twelve point half-log compound concentration–response curves, with a top concentration of 100 μM (1 mM for fragments), were generated from 10 mM (100 mM for fragments) stocks of compounds solubilized in DMSO using an Echo 555 (Labcyte Inc., Sunnyvale, CA). 10 μL of enzyme (MAT2a and inorganic pyrophosphatase) and 10 μL of substrate (methionine and ATP) were added to the compound plate, and reaction was incubated at room temperature for 90 min. Final concentrations in the reaction mix were 40 nM MAT2a, 1 μg/mL inorganic pyrophosphatase, 20 μM methionine, and 70 μM ATP. Enzyme reaction was stopped by addition of 40 μL of BIOMOL GREEN reagent to each well and incubated for 20 min. Absorbance at 620 nm was read using an Envision plate reader. IC<sub>50</sub> values were calculated using a Genedata Screener (Genedata AG, Basel, Switzerland).

**SDMA Imaging.** HCT116 KO-MTAP cells were cultured in cell media composed of McCoys media (Sigma no. M8403), 10% (v/v) fetal calf serum, and 1% (v/v) L-glutamine. After harvesting, cells were dispensed into black, 384-well Costar plates (no. 3712, Corning) to give 2000 cells per well in a total volume of 40 μL of cell media. Test compounds and reference controls were dosed directly into the cell plates using a Labcyte Echo 555 acoustic dispenser following a 12 point half-log compound concentration–response with a top concentration of 30 μM.

The cell plates were then incubated for 48 h at 37 °C before being fixed by the addition of 40 μL of 8% paraformaldehyde in PBS/A (4% final concentration), followed by a 10 min rt incubation. Plates were then washed twice with 150 μL of PBS using a BioTek ELx406 platelasher, permeabilized for 10 min with 20 μL/well 0.1% saponin in PBS, washed again, and blocked with 20 μL/well 2% BSA in PBS-T (Sigma no. A8022) for 1 h at rt.

Primary anti-SDMA histone 4 antibody (Milipore no. 07-947) was diluted 1:1000 in PBS-T + 0.05% BSA, 20 μL added per well, and plates were incubated at 4 °C overnight. Cell plates were washed 3× with 200 μL of PBS/T, and then 20 μL of 1:500 dilution in assay buffer of Alexa Fluor 488 goat anti-rabbit IgG secondary antibody (Thermo no. A11008), with a 1:1000 dilution of Hoechst 33342, was added per well. Following a 1 h incubation at rt, plates were washed 3× with 200 μL of PBS/T, and 40 μL of PBS without Ca, Mg, and Na Bicarb (Gibco no. 14190-094) was added per well.

Stained cell plates were covered with black seals and then read on the Cell Insight imaging platform (Thermo Scientific), with a 10× objective. The primary channel (Hoechst blue fluorescence 405 nm, BGRFR\_386\_23) is used to autofocus and to count the number of events (this will provide information about cytotoxicity of the compounds tested). The secondary channel (Green 488 nm, BGRFR\_485\_20) measures SDMA staining. Data were analyzed, and IC<sub>50</sub> values were calculated using Genedata Screener software.

After normalization to maximum signal/top (vehicle control) and minimum signal/bottom (30 μM of PRMT5 inhibitor GSK-3326595,<sup>22</sup> CAS no. 1616392-22-3), data were fitted to a four-parameter (Hill) IC<sub>50</sub> model.

**Proliferation Assay.** HCT116 KO MTAP cells were cultured in cell media composed of McCoys media (Sigma no. M8403), 10% (v/v) fetal calf serum, and 1% (v/v) L-glutamine. After harvesting, cells were dispensed into black, 384-well Costar plates (no. 3712, Corning) to give 400 cells per well in a total volume of 40 μL of cell media. Test compounds and reference controls were dosed directly into the cell plates using a Labcyte Echo 555 acoustic dispenser following a 12 point duplicate half-log compound concentration–response with a top concentration of 30 μM.

A day 0 plate is created in parallel but not dosed, after plating 4 μL of Alamar Blue (Thermo no. DAL1100) and incubating for 3 h at 37 °C, 5% CO<sub>2</sub>. Following incubation, plates are read using an EnVision plate reader with fluorescence excitation wavelength of 540–570 nm (peak excitation is 570 nm), fluorescence emission at 580–610 nm (peak emission is 585 nm).

The dosed cell plates were then incubated for 5 d at 37 °C before adding Alamar blue and being read in the Envision following the same protocol as for first plate. Data were analyzed, and IG<sub>50</sub> values were calculated using Genedata Screener software by normalizing to plate 0.

## ■ ASSOCIATED CONTENT

### Supporting Information

The Supporting Information is available free of charge at <https://pubs.acs.org/doi/10.1021/acs.jmedchem.1c00067>.

Supplementary figures and table; extended methods (PDF)

Molecular formula strings (CSV)

## Accession Codes

Crystal structures of MAT2a small molecule complexes have been deposited in the PDB under the following accession codes: **1** (7bhr), **2** (7bhs), **5** (7bht), **26** (7bhu), **28** (7bhv), **29** (7bhw), **31** (7bhx). Authors will release the atomic coordinates and experimental data upon article publication.

## ■ AUTHOR INFORMATION

### Corresponding Authors

**Claudia De Fusco** – Discovery Sciences, R&D, AstraZeneca, Cambridge CB4 0WG, United Kingdom; [orcid.org/0000-0001-8807-4976](https://orcid.org/0000-0001-8807-4976); Email: [claudia.defusco@gmail.com](mailto:claudia.defusco@gmail.com)

**Marianne Schimpl** – Discovery Sciences, R&D, AstraZeneca, Cambridge CB4 0WG, United Kingdom; [orcid.org/0000-0003-2284-5250](https://orcid.org/0000-0003-2284-5250); Email: [marianne.schimpl@astrazeneca.com](mailto:marianne.schimpl@astrazeneca.com)

### Authors

**Ulf Börjesson** – Discovery Sciences, R&D, AstraZeneca, Gothenburg SE-431 83, Sweden

**Tony Cheung** – Oncology R&D, AstraZeneca, Boston, Massachusetts 02451, United States

**Iain Collie** – Discovery Sciences, R&D, AstraZeneca, Cambridge CB4 0WG, United Kingdom

**Laura Evans** – Oncology R&D, AstraZeneca, Cambridge CB4 0WG, United Kingdom

**Priyanka Narasimhan** – Discovery Sciences, R&D, AstraZeneca, Cambridge CB4 0WG, United Kingdom

**Christopher Stubbs** – Discovery Sciences, R&D, AstraZeneca, Cambridge CB4 0WG, United Kingdom

**Mercedes Vazquez-Chantada** – Discovery Sciences, R&D, AstraZeneca, Cambridge CB4 0WG, United Kingdom

- David J. Wagner – Oncology R&D, AstraZeneca, Boston, Massachusetts 02451, United States; [orcid.org/0000-0002-5805-930X](https://orcid.org/0000-0002-5805-930X)
- Michael Grondine – Oncology R&D, AstraZeneca, Boston, Massachusetts 02451, United States
- Matthew G. Sanders – Oncology R&D, AstraZeneca, Cambridge CB4 0WG, United Kingdom
- Sharon Tentarelli – Oncology R&D, AstraZeneca, Boston, Massachusetts 02451, United States
- Elizabeth Underwood – Discovery Sciences, R&D, AstraZeneca, Cambridge CB4 0WG, United Kingdom
- Argyrides Argyrou – Discovery Sciences, R&D, AstraZeneca, Cambridge CB4 0WG, United Kingdom; [orcid.org/0000-0003-3141-9122](https://orcid.org/0000-0003-3141-9122)
- James M. Smith – Oncology R&D, AstraZeneca, Cambridge CB4 0WG, United Kingdom; [orcid.org/0000-0002-6750-265X](https://orcid.org/0000-0002-6750-265X)
- James T. Lynch – Oncology R&D, AstraZeneca, Cambridge CB4 0WG, United Kingdom
- Elisabetta Chiarparin – Oncology R&D, AstraZeneca, Cambridge CB4 0WG, United Kingdom; [orcid.org/0000-0002-2998-1346](https://orcid.org/0000-0002-2998-1346)
- Graeme Robb – Oncology R&D, AstraZeneca, Cambridge CB4 0WG, United Kingdom; [orcid.org/0000-0002-4531-4375](https://orcid.org/0000-0002-4531-4375)
- Sharan K. Bagal – Oncology R&D, AstraZeneca, Cambridge CB4 0WG, United Kingdom
- James S. Scott – Oncology R&D, AstraZeneca, Cambridge CB4 0WG, United Kingdom; [orcid.org/0000-0002-2263-7024](https://orcid.org/0000-0002-2263-7024)

Complete contact information is available at:  
<https://pubs.acs.org/10.1021/acs.jmedchem.1c00067>

### Author Contributions

The manuscript was written through contributions of all authors. All authors have given approval to the final version of the manuscript.

### Notes

The authors declare the following competing financial interest(s): At the time of writing, all authors were employees of, and owned shares in, AstraZeneca PLC.

### ACKNOWLEDGMENTS

The authors gratefully acknowledge Nin Guan's valued contribution to preparing samples for mass spectrometry analysis; Crystal Brown's significant effort in carrying out compound tolerability and efficacy studies; Jason Breed's help with crystallographic data collection; Eva Lenz and Paul Davey for compound purity checks; and Ian Storer's contributions regarding the manuscript.

### ABBREVIATIONS USED

ATP, adenosine triphosphate; AUC, area under the curve; CL, clearance; DCM, dichloromethane; DMPK, drug metabolism and pharmacokinetics; ER, efflux ratio; hep, hepatocyte; KHMDs, potassium bis(trimethylsilyl)amide; LE, ligand efficiency; LLE, ligand lipophilic efficiency; MAT, methionine adenosyltransferase; MDCK, Madin–Darby canine kidney; MTA, methylthioadenosine;  $P_{app}$ , apparent permeability; po, *per os* (oral dosing); PyBOP, benzotriazol-1-yl-oxytripyrrolidinophosphonium hexafluorophosphate; SAM, S-adenosylmethionine; sc, subcutaneous; SDMA,

symmetric dimethyl arginine; SFC, supercritical fluid chromatography;  $S_NAr$ , aromatic nucleophilic substitution; SPR, surface plasmon resonance;  $t_{1/2}$ , half-life;  $V_{ss}$ , volume of distribution at steady state

### REFERENCES

- (1) Lu, S. C.; Mato, J. M. S-adenosylmethionine in liver health, injury, and cancer. *Physiol. Rev.* **2012**, *92* (4), 1515–1542.
- (2) Ramani, K.; Mato, J. M.; Lu, S. C. Role of methionine adenosyltransferase genes in hepatocarcinogenesis. *Cancers* **2011**, *3* (2), 1480–1497.
- (3) McDonald, E. R., III; de Weck, A.; Schlabach, M. R.; Billy, E.; Mavrakis, K. J.; Hoffman, G. R.; Belur, D.; Castelletti, D.; Frias, E.; Gampa, K.; Golji, J.; Kao, I.; Li, L.; Megel, P.; Perkins, T. A.; Ramadan, N.; Ruddy, D. A.; Silver, S. J.; Sovath, S.; Stump, M.; Weber, O.; Widmer, R.; Yu, J.; Yu, K.; Yue, Y.; Abramowski, D.; Ackley, E.; Barrett, R.; Berger, J.; Bernard, J. L.; Billig, R.; Brachmann, S. M.; Buxton, F.; Caothien, R.; Caushi, J. X.; Chung, F. S.; Cortés-Cros, M.; deBeaumont, R. S.; Delaunay, C.; Desplat, A.; Duong, W.; Dwsoske, D. A.; Eldridge, R. S.; Farsidjani, A.; Feng, F.; Feng, J.; Flemming, D.; Forrester, W.; Galli, G. G.; Gao, Z.; Gauter, F.; Gibaja, V.; Haas, K.; Hattenberger, M.; Hood, T.; Hurov, K. E.; Jagani, Z.; Jenal, M.; Johnson, J. A.; Jones, M. D.; Kapoor, A.; Korn, J.; Liu, J.; Liu, Q.; Liu, S.; Liu, Y.; Loo, A. T.; Macchi, K. J.; Martin, T.; McAllister, G.; Meyer, A.; Mollé, S.; Pagliarini, R. A.; Phadke, T.; Repko, B.; Schouwey, T.; Shanahan, F.; Shen, Q.; Stamm, C.; Stephan, C.; Stucke, V. M.; Tiedt, R.; Varadarajan, M.; Venkatesan, K.; Vitari, A. C.; Wallroth, M.; Weiler, J.; Zhang, J.; Mickanin, C.; Myer, V. E.; Porter, J. A.; Lai, A.; Bitter, H.; Lees, E.; Keen, N.; Kauffmann, A.; Stegmeier, F.; Hofmann, F.; Schmelzle, T.; Sellers, W. R. Project DRIVE: A Compendium of Cancer Dependencies and Synthetic Lethal Relationships Uncovered by Large-Scale, Deep RNAi Screening. *Cell* **2017**, *170* (3), 577–592.
- (4) Kryukov, G. V.; Wilson, F. H.; Ruth, J. R.; Paulk, J.; Tsherniak, A.; Marlow, S. E.; Vazquez, F.; Weir, B. A.; Fitzgerald, M. E.; Tanaka, M.; Bielski, C. M.; Scott, J. M.; Dennis, C.; Cowley, G. S.; Boehm, J. S.; Root, D. E.; Golub, T. R.; Clish, C. B.; Bradner, J. E.; Hahn, W. C.; Garraway, L. A. MTAP deletion confers enhanced dependency on the PRMT5 arginine methyltransferase in cancer cells. *Science (Washington, DC, U. S.)* **2016**, *351* (6278), 1214–8.
- (5) Marjon, K.; Cameron, M. J.; Quang, P.; Clasquin, M. F.; Mandley, E.; Kunii, K.; McVay, M.; Choe, S.; Kernytsky, A.; Gross, S.; Konteatis, Z.; Murtie, J.; Blake, M. L.; Travins, J.; Dorsch, M.; Biller, S. A.; Marks, K. M. MTAP Deletions in Cancer Create Vulnerability to Targeting of the MAT2A/PRMT5/RIOK1 Axis. *Cell Rep.* **2016**, *15* (3), 574–587.
- (6) Zhang, H.; Chen, Z.-H.; Savarese, T. M. Codeletion of the genes for p16INK4, methylthioadenosine phosphorylase, interferon- $\alpha$ 1, interferon- $\beta$ 1, and other 9p21 markers in human malignant cell lines. *Cancer Genet. Cytogenet.* **1996**, *86* (1), 22–28.
- (7) Albers, E. Metabolic characteristics and importance of the universal methionine salvage pathway recycling methionine from 5'-methylthioadenosine. *IUBMB Life* **2009**, *61* (12), 1132–1142.
- (8) Lombardini, J. B.; Coulter, A. W.; Talalay, P. Analogues of Methionine as Substrates and Inhibitors of the Methionine Adenosyltransferase Reaction. *Mol. Pharmacol.* **1970**, *6* (5), 481–499.
- (9) Lombardini, J. B.; Sufrin, J. R. Chemotherapeutic potential of methionine analogue inhibitors of tumor-derived methionine adenosyltransferases. *Biochem. Pharmacol.* **1983**, *32* (3), 489–495.
- (10) Quinlan, C. L.; Kaiser, S. E.; Bolaños, B.; Nowlin, D.; Grantner, R.; Karlicek-Bryant, S.; Feng, J. L.; Jenkinson, S.; Freeman-Cook, K.; Dann, S. G.; Wang, X.; Wells, P. A.; Fantin, V. R.; Stewart, A. E.; Grant, S. K. Targeting S-adenosylmethionine biosynthesis with a novel allosteric inhibitor of Mat2A. *Nat. Chem. Biol.* **2017**, *13* (7), 785–792.
- (11) Murray, B.; Antonyuk, S. V.; Marina, A.; Van Liempd, S. M.; Lu, S. C.; Mato, J. M.; Hasnain, S. S.; Rojas, A. L. Structure and

function study of the complex that synthesizes S-adenosylmethionine. *IUCrJ* **2014**, *1*, 240–249.

(12) Konteatis, Z. D.; Sui, Z.; Travins, J. M.; Ye, Z. Pyrazolo[1,5-a]pyrimidin-7(4H)-ones as inhibitors of cellular metabolic processes and their preparation. Patent US20180079753 A1, 2018.

(13) Konteatis, Z. D.; Li, M.; Reznik, S. K.; Sui, Z.; Travins, J. M. Preparation of azaheterobicyclic inhibitors of MAT2A and methods of use for treating cancer. Patent WO2020139992 A1, 2020.

(14) Konteatis, Z. D.; Li, M.; Liu, P.; Medeiros, M.; Reznik, S. K.; Sui, Z.; Travins, J. M.; Popovici-Muller, J.; Zhou, S.; Ma, G. Preparation of heterobicyclic compounds as inhibitors of MAT2A and methods of use for treating cancer. Patent WO2019191470 A1, 2019.

(15) Erlanson, D. A.; Fesik, S. W.; Hubbard, R. E.; Jahnke, W.; Jhoti, H. Twenty years on: the impact of fragments on drug discovery. *Nat. Rev. Drug Discovery* **2016**, *15* (9), 605–619.

(16) Jacquemard, C.; Kellenberger, E. A bright future for fragment-based drug discovery: what does it hold? *Expert Opin. Drug Discovery* **2019**, *14* (5), 413–416.

(17) Boyd, S. M.; de Kloe, G. E. Fragment library design: efficiently hunting drugs in chemical space. *Drug Discovery Today: Technol.* **2010**, *7* (3), e173–e180.

(18) Cheron, N.; Jasty, N.; Shakhnovich, E. I. OpenGrowth: An Automated and Rational Algorithm for Finding New Protein Ligands. *J. Med. Chem.* **2016**, *59* (9), 4171–4188.

(19) Abel, R.; Young, T.; Farid, R.; Berne, B. J.; Friesner, R. A. Role of the active-site solvent in the thermodynamics of factor Xa ligand binding. *J. Am. Chem. Soc.* **2008**, *130* (9), 2817–2831.

(20) Young, T.; Abel, R.; Kim, B.; Berne, B. J.; Friesner, R. A. Motifs for molecular recognition exploiting hydrophobic enclosure in protein-ligand binding. *Proc. Natl. Acad. Sci. U. S. A.* **2007**, *104* (3), 808–813.

(21) As this manuscript was in preparation a patent application (Alam, M.; Cleary, L.; Fleury, M.; Pei, Z.; Steel, R.; Sutton, J.; Knox, J. E.; Newby, Z. E. R. 2-Oxoquinazoline derivatives as methionine adenosyltransferase 2A inhibitors and their preparation. Patent WO2020123395 A1, 2020) from Ideaya was published on the chemical series described in this paper.

(22) Duncan, K. W.; Chesworth, R.; Boriack-Sjodin, P. A.; Munchhof, M. J.; Jin, L.; Penebre, E.; Barbash, O. I. Prmt5 Inhibitors and Uses Thereof. Patent WO2016022605 A1, 2016.

## ■ NOTE ADDED AFTER ASAP PUBLICATION

A new reference 11 was added May 5, 2021.